

DOI: 10.1002/((please add manuscript number))

Article type: Communication

Amorphous TiO₂ Shells: A Vital Elastic Buffering Layer on Silicon Nanoparticles for High-Performance and Safe Lithium Storage

Jianping Yang, Yunxiao Wang, Wei Li, Lianjun Wang, Yuchi Fan, Wan Jiang, Wei Luo, Yang Wang, Biao Kong, Cordelia Selomulya, Hua Kun Liu, Shi Xue Dou and Dongyuan Zhao**

Dr. J. P. Yang, Prof. L. J. Wang, Dr. Y. C. Fan, Prof. W. Jiang, Dr. W. Luo,

State Key Laboratory for Modification of Chemical Fibers and Polymer Materials, College of Materials Science and Engineering, Donghua University, Shanghai 201620, P. R. China.

E-mail: wluo@dhu.edu.cn

Dr. Y. X. Wang, Prof. H. K. Liu, Prof. S. X. Dou

Institute for Superconducting & Electronic Materials, Australian Institute of Innovative Materials, University of Wollongong, Innovation Campus, Squires Way, North Wollongong, NSW 2500, Australia

Dr. W. Li, Prof. D. Y. Zhao

Department of Chemistry, Laboratory of Advanced Materials, Fudan University, Shanghai 200433, P. R. China

E-mail: dyzhao@fudan.edu.cn

This is the author manuscript accepted for publication and has undergone full peer review but has not been through the copyediting, typesetting, pagination and proofreading process, which may lead to differences between this version and the [Version of Record](#). Please cite this article as [doi: 10.1002/adma.201700523](#).

This article is protected by copyright. All rights reserved.

Y. Wang, Dr. B. Kong, Prof. C. Selomulya, Prof. D. Y. Zhao

Department of Chemical Engineering, Monash University, Clayton, Victoria 3800, Australia

Keywords: core-shell structure, sol-gel coating, titanium oxide, lithium ion batteries, silicon nanoparticles

Smart surface coatings of silicon nanoparticles are shown to be good examples for dramatically improving the cyclability of lithium ion batteries. Most coating materials, however, face significant challenges including a low initial Coulombic efficiency, tedious processing and safety assessment. Here, we demonstrate a facile sol-gel strategy to synthesize amorphous TiO_2 -encapsulated commercial Si nanoparticles with core-shell structures that show greatly superior electrochemical performance and high-safety lithium storage. The amorphous TiO_2 shell (~ 3 nm) shows elastic behavior during lithium discharge and charge processes, maintaining high structural integrity. Interestingly, it is found that the amorphous TiO_2 shells offer superior buffering properties compared to crystalline TiO_2 layers for unprecedented cycling stability. Moreover, accelerating rate calorimetry testing reveals that the TiO_2 -encapsulated Si nanoparticles are safer than conventional carbon-coated Si-based anodes.

1. Introduction

The exploitation of advanced lithium-ion batteries (LIBs) with high energy density and long-term cycling stability is of crucial importance to meet the growing requirements for next-generation energy storage devices.^[1] Silicon (Si) has been received remarkable attention as a promising anode material for rechargeable LIBs, which is ascribed to its unparalleled theoretical gravimetric capacity of $\sim 4200 \text{ mA h g}^{-1}$.^[2] The main challenges for silicon anodes, however, are structural degradation and unstable solid electrolyte interphase (SEI) growth caused by the large volume expansion ($\sim 400\%$) during lithium insertion and the continuous occurrence of side reactions with electrolyte, which

lead to the pulverization of electrode materials, severely decreasing the cycle life of Si-based anodes.^[3]

Rational design of the electrode structures is considered a good way to improve the performance of silicon anodes, for instance, the synthesis of silicon nanostructures with diversified morphologies and hybridization with conducting matrixes.^[2a, 4] Various silicon nanostructures such as nanocrystals,^[5] nanotubes,^[6] nanowires,^[7] and porous spheres,^[8] have been obtained to extend the cycle lifetime of Si anodes.^[9] The fabrication of these silicon nanostructures, however, usually involves toxic reagents, complex reactions, or a high temperature chemical vapor deposition process.^[10] Another promising approach to achieve high performance lithium storage is based on the core-shell and yolk-shell structures.^[3a, 11] The surface coating layers not only improve the conductivity of electrodes, but also avoid direct contact between the silicon and the electrolyte, thus reducing the uncontrollable growth of the SEI film, which results in a remarkable improvement in cycling stability.^[12] In the case of most coating layers (e.g., amorphous carbon and graphene), however, it is also frustrating that the very low initial Coulombic efficiency (ICE < 80 %) that results from the coating further hinders the advance of various Si-based composites into practical application.^[13] Recently, titanium oxides (TiO₂) with crystalline rutile and anatase phases have been proposed as promising and favorable substitutes for carbonaceous shells.^[14] It is well known that TiO₂ undergoes only slight volume expansion upon lithiation (< 4 %), and the resultant lithiated TiO₂ during discharge can promote the electrical conductivity of the electrode. On the other hand, the lithiated TiO₂ layers are able to promote better safety due to their thermal stability, which would suppress the exothermic reactions between the highly lithiated Si phase and the electrolyte solution.^[15] Most recently, outer layers of amorphous TiO₂ have been shown to be outstanding

compared to the other coatings due to their intrinsically isotropic nature and open active diffusion channels, facilitating Li-ion mobility, and ionic and electronic diffusion, leading to high ion accessibility and enhanced power and energy densities of the inner hosts.^[16] Using an amorphous TiO₂ coating, therefore, is expected to be a superior strategy for optimizing the electrochemical properties of Si nanoparticles.

Herein, we report a facile sol-gel approach to produce amorphous TiO₂ coated commercial Si nanoparticle core-shell nanostructures (denoted as Si@a-TiO₂). The amorphous TiO₂ shells show elastic behavior with strain relaxation, thereby maintaining the integrity of the anode and stabilizing the volume expansion during lithium insertion and extraction. On the other hand, the amorphous TiO₂ layers can offer high lithium ion diffusivity due to the absence of long-range order and the presence of defects, thus increasing the accessibility to Li and electrochemical reactivity. As a consequence, the Si@a-TiO₂ electrode delivers a high initial Coulombic efficiency (ICE) of ~ 86.1 %, a specific capacity of ~ 1720 mA·h·g⁻¹ over 200 cycles at a current density of 420 mA·g⁻¹, with a high retained capacity of 812 mA·h·g⁻¹ at the rate of 8.4 A·g⁻¹, and better safety performance than that of the carbon-coated Si anodes, according to the accelerating rate calorimetry tests. We believe that this core-shell Si@a-TiO₂ nanocomposite is very promising and paves the way for safe and high-performance Si-based LIBs.

2. Results and discussion

The amorphous TiO₂ shells are conformally deposited on commercial Si nanoparticles *via* a kinetics-controlled sol-gel coating approach using titanium isopropylate as a precursor in an alkaline

alcohol system (**Figure 1a** and Figure S1 in the Supporting Information). Moreover, titanium isopropylate displays a much slower hydrolysis rate in pure ethanol solution, guaranteeing the uniform growth of the amorphous TiO_2 .^[17] The formation of the core-shell nanoparticles was confirmed by dynamic light scattering (DLS) measurements, as the average hydrodynamic diameter is increased after coating (Figure S1b). The tap density of the resultant Si@a-TiO_2 core-shell nanoparticles ($0.60 \text{ g}\cdot\text{cm}^{-3}$) is significantly higher than that of the pristine Si nanoparticles ($0.15 \text{ g}\cdot\text{cm}^{-3}$) (Figure S1c), resulting in a high volumetric capacity, which is a key parameter for practical application.

The Si nanoparticles display a predominant size of $\sim 100 \text{ nm}$ with a smooth and crystalline surface, as observed by scanning electron microscopy (SEM) and high-resolution transmission electron microscopy (HRTEM) images (Figure S1). The resultant core-shell Si@a-TiO_2 nanoparticles inherit the spherical morphology of Si nanoparticle cores but with rough surfaces, suggesting the deposition of TiO_2 nano-grains (Figure 1b). The transmission electron microscope (TEM) image demonstrates that the Si nanoparticles are uniformly encapsulated by the amorphous TiO_2 layers (Figure 1c). High-magnification TEM images of the Si@a-TiO_2 nanospheres further confirm that large numbers of tiny TiO_2 nano-grains are uniformly dispersed on the individual Si nanoparticles (Figure 1d). HRTEM observations not only clearly make manifest that the Si nanoparticle cores are well-crystallized and conformally coated by a thin TiO_2 layer with the thickness of $\sim 3 \text{ nm}$, but also disclose the amorphous nature of the TiO_2 shells (Figure 1e). Scanning TEM (STEM) images of a single Si@a-TiO_2 nanoparticle, combined with the elemental mapping images of Si, O, and Ti, reveal the well-defined core-shell structure with homogenous distribution of a thin TiO_2 layer on the Si nanoparticle surface (Figure 1f). The presence of Si, Ti, and O elements in the nanoparticles is further confirmed by the energy-

dispersive X-ray (EDX) spectrum (Figure S2), yielding $\sim 89\%$ silicon by mass, which is consistent with the X-ray photoelectron spectroscopy (XPS) results.

The XPS survey spectrum of the Si@a-TiO₂ nanoparticles shows a distinct peak of Ti 2p and the decreased intensity of Si 2s and Si 2p peaks compared to the pristine Si nanoparticles, suggesting that the Si cores are well encapsulated by the TiO₂ shells (Figure 2a). In addition, the high-resolution XPS spectrum shows that Ti 2p peaks are centered at 458.5 and 464.2 eV, assigned to Ti 2p_{3/2} and 2p_{1/2} of TiO₂, respectively (Figure S3). Moreover, the O 1s high-resolution XPS spectrum can be deconvoluted into two single-peaks corresponding to O-H (531.7 eV), and Ti-O (530.4 eV), revealing the presence of Ti-OH groups in the amorphous TiO₂ matrix (Figure 2b). The amorphous property of the TiO₂ shells is also confirmed by the X-ray diffraction (XRD) patterns (Figure 2c and Figure S4), in which only the diffraction peaks from crystalline Si can be observed and no other signals assignable to TiO₂ are detected. The nitrogen sorption isotherms of the Si@a-TiO₂ nanoparticles present typical type IV curves with a sharp capillary condensation step in the high pressure range, which can be attributed to the aggregated nanoparticle structure (Figure 2d). The Brunauer-Emmett-Teller (BET) surface areas of the pristine Si and Si@a-TiO₂ nanoparticles are calculated to be 28, and 35 m²·g⁻¹, respectively. Moreover, the Si@a-TiO₂ nanoparticles present indistinct pore size distribution, and high pore volume of 0.104 cm³·g⁻¹.

During the first cathodic scan of the Si@a-TiO₂ nanoparticles, a suppressed broad peak at 1.25 V is observed, which corresponds to formation of SEI layers (Figure 3a). Meanwhile, a cathodic peak evolves at 0.01 V, which is attributed to the background current. In the following scans, a peak at 0.185 V gradually intensifies, which is ascribed to the formation of amorphous Li-Si phases. During the charge process, a sluggish anodic peak appears at 0.54 V during the initial scan; and an additional

peak at ~ 0.14 V evolves as cycling proceeds. The peaks correspond to the delithiation of Li-Si phases to amorphous Si, and the reinforced peaks indicate the improved delithiation kinetics. Therefore, the amorphous TiO_2 coating on the surface, which contains disordered structures and defects that promote Li insertion, expands the potential range and eliminates the plateaus for Li and TiO_2 reactions, leaving only cathodic/anodic peaks that are typical of Si anodes. It is noteworthy that extra pairs of peaks appear at 1.75 V during discharge and at 2.06 V in the charge process with high repetition. They correspond to the redox reaction of $\text{Ti}^{4+}/\text{Ti}^{3+}$ in the anatase TiO_2 shells (Figures 3b, S4, and S5), likely inducing the degradation of the core-shell structure. In contrast, there are two exceptional anodic peaks that appear in the initial discharge scan; the hump at 1.1 V is ascribed to the irreversible phase transition from the amorphous TiO_2 to cubic $\text{Li}_2\text{Ti}_2\text{O}_4$, which possesses much lower diffusion activation barrier (0.257 eV) than that for anatase (0.5 eV).^[18] The amorphous TiO_2 shells, therefore, could facilitate rapid lithiation/delithiation processes and realize high ion accessibility to the Si cores as well. As shown in Figure 3c, unlike the steep capacity decline of the pristine Si nanoparticles, it is obvious that both of the amorphous and the anatase TiO_2 coatings are able to enhance the electrochemical performance of the electrodes in term of cycling stability and specific capacity, resulting from the improved conductivity and toleration for the volume variation of Si cores. The Si@c- TiO_2 and Si@a- TiO_2 nanoparticles deliver reversible capacity of 2200 and 3061 $\text{mA}\cdot\text{h}\cdot\text{g}^{-1}$ in the first cycle, respectively, corresponding to initial Coulombic efficiencies (ICE) of 79 and 86.1 %. The high ICE value of the Si@a- TiO_2 is critical and essential for practical application in full-cell type batteries. In addition, outstanding cycling stability is observed for the Si@a- TiO_2 nanoparticles, as suggested in the galvanostatic discharge and charge voltage profiles for different cycles (Figure S6). Furthermore, high reversible capacity and sustainable capacity retention can be achieved for the

Si@a-TiO₂ composite, which delivers a stable capacity of $\sim 1720 \text{ mA}\cdot\text{h}\cdot\text{g}^{-1}$ over 200 cycles, in comparison with retention of 150 and 88 $\text{mA}\cdot\text{h}\cdot\text{g}^{-1}$ for the Si@c-TiO₂ and Si nanoparticles, respectively (Table S1). Moreover, the Si@a-TiO₂ composite shows a high areal capacity of $1.07 \text{ mA h cm}^{-2}$ over 200 cycles (Figure S7). The superiority of the core-shell Si@a-TiO₂ composites is also manifested via their prevailing rate capability in Figure 3d. The reversible capacities of 3420, 3441, 3000, 2518, 1083, and 812 $\text{mA}\cdot\text{h}\cdot\text{g}^{-1}$ are achieved at various current rate from 0.14 to $8.4 \text{ A}\cdot\text{g}^{-1}$, corresponding to much lower capacities of 2273, 2090, 1667, 1046, 493, and 33 $\text{mA}\cdot\text{h}\cdot\text{g}^{-1}$ for Si@c-TiO₂ (Figure S8). When charged again at $0.42 \text{ A}\cdot\text{g}^{-1}$, a much higher reversible capacity of $2614 \text{ mA}\cdot\text{h}\cdot\text{g}^{-1}$ for the Si@a-TiO₂ nanoparticles could be recovered compared to $1693 \text{ mA}\cdot\text{h}\cdot\text{g}^{-1}$ for the Si@c-TiO₂ nanoparticles. Electrochemical impedance spectroscopy (EIS) measurements were also carried out on the electrodes after rate capability testing (Figure S9). The Si@a-TiO₂ nanoparticles had the lowest resistance, which confirms the fast Li kinetics and highly conductive solid electrolyte interphase (SEI) film that was formed due to the aid of the amorphous TiO₂ shells.

The structural evolution of the core-shell Si@a-TiO₂ nanoparticles during the initial lithiation and delithiation processes were observed *via ex-situ* TEM measurements. As shown in Figure 4a and 4b, the amorphous TiO₂ coating is robust and able to tolerate large volume expansion of the Si nanoparticles without particle pulverization and structural rupture. During cycling, the Si@a-TiO₂ nanoparticles are expected to retain the original core-shell structure; and a thicker and thicker SEI film is formed around the amorphous TiO₂ surface. The corresponding TEM results well confirm this speculation, in which the Si nanoparticle cores undergo huge volume expansion, leading to distortion of the Si spheres during the first discharge process. Surprisingly, it should be pointed out that the distorted and lithiated Si@a-TiO₂ nanoparticles still retain the core-shell structure with

uniform SEI films present on the outside, implying that the amorphous TiO_2 shells are robust enough to tolerate volume variation of the Si cores. Furthermore, another interesting phenomenon should be noted that voids are created in the distorted Si nanoparticles (Figure 4b and Figure S10A-A5). The increased voids in lithiated Si@a-TiO_2 nanoparticles thus add more space to buffer the volume expansion, contributing to the structural integrity.^[19] As predicted, the core-shell structures of the Si@a-TiO_2 nanoparticles can be regained after the first delithiation process and the diameter decreases from 188 to 106 nm (Figure 4b). Optical, SEM and TEM images (Figure 4c-g) of the Si@a-TiO_2 nanoparticle electrodes after 200 cycles exhibit compact electrodes without cracking. The Si nanoparticles are still firmly encapsulated by the amorphous TiO_2 coating layers with well-defined spherical structures, clearly demonstrating that the Si@a-TiO_2 nanoparticles are stable enough to withstand the volume expansion/shrinkage during lithium insertion and extraction processes. In the case the Si@c-TiO_2 nanoparticles, the rigid crystalline TiO_2 shells cannot accommodate the volume expansion during cycling, and therefore, the Si@c-TiO_2 nanoparticles are gradually pulverized and completely lose their spherical structure after the long-term cycling (Figure S11). Significantly, with the effects of the amorphous TiO_2 shells, the original structure of the Si@a-TiO_2 nanoparticles is likely to be preserved over prolonged cycling, thereby leading to good cycling stability and high capacity retention.

Accelerating rate calorimetry (ARC) tests were further carried out to investigate the safety properties of the Si@a-TiO_2 nanoparticle electrodes. As shown in Figure 3e, the decomposition of the electrolytes by itself is exothermic. The self-heating due to electrolyte decomposition is dramatic in the range from 175 - 275 °C. It is interesting that the Si@a-TiO_2 nanoparticles show similar exothermic features to the bare electrolytes at a consistent self-heating rate below 275 °C,

indicating that a robust and thermally stable SEI film is formed on the nanoparticle surface. This SEI film is partially responsible for the excellent capacity retention during long-term cycling. A mild exothermic reaction resulting in self-heating for the Si@a-TiO₂ nanoparticles occurs at ~ 285 °C. In sharp contrast, the results for the Si@C nanoparticles (Figure S12) show that two exothermic reactions evolve with an onset temperature of 228.5 and 234 °C, respectively. The exothermic reactions correspond to the decomposition of the metastable components of the SEI and their reaction with electrolyte to form stable products. Therefore, in comparison with the carbon shells, the more stable and robust SEI films on the amorphous TiO₂ layers are responsible for suppressing any obvious exothermic reaction up to 285 °C, resulting in a higher battery safety.

3. Conclusions

In summary, we have demonstrated a conformal growth of amorphous TiO₂ shell as an appealing encapsulation layer for stabilizing the silicon nanoparticle anode. Compared with other coating materials, such as graphene, carbon, silica and polymer, this conformal amorphous TiO₂ completely surrounds the Si nanoparticles and imparts the following advantages. First, it is built up by a facile sol-gel route at low reaction temperature without an annealing treatment, enabling the fabrication of Si@a-TiO₂ nanoparticles at low cost. Second, the amorphous TiO₂ shells, which give rise to much lower Li⁺ diffusion resistances and faster transport capacity, more importantly deliver much better safety performance than the carbon coated Si nanoparticles. Third, the amorphous and flexible TiO₂ shells show elastic behavior during lithium discharge and charge processes, remaining undamaged and confining all the Si pieces within. Fourth, the SEI film is expected to mainly form a stable on the surface of the amorphous TiO₂ and prevent electrolyte impregnation within the sealed Si core. Finally, these designed Si@a-TiO₂ nanoparticles have a high amount of silicon (89 wt% and 0.621 mg

cm⁻²) and render a decent electrochemical performance, including large initial Coulombic efficiency of 86.1 %, outstanding reversible capacity of ~ 1720 mA·h·g⁻¹ even after 200 cycles and excellent cycling stability. Coupled with a simple fabrication protocol as well as commercially available raw materials, our findings may provide unprecedented opportunities for realizing the design of safe lithium ion batteries with high performance.

Supporting Information

Supporting Information is available from the Wiley Online Library or from the author.

Acknowledgements

This project was funded by the National Natural Science Foundation of China (No. 51402049 and No. 51432004), the Shanghai Committee of Science and Technology, China (No. 14ZR1400600 and No. 17ZR1401000), the Fundamental Research Funds for the Central Universities (No. 2232015D3-06), and the Programme of Introducing Talents of Discipline to Universities (No.111-2-04). Dr. J. P. Yang is grateful for financial support from State Key Laboratory for Modification of Chemical Fibers and Polymer Materials, Donghua University. We also thank the Australian Research Council (ARC) (DP160102627), the Commonwealth of Australia through the Automotive Australia 2020 Cooperative Research Centre (Auto CRC 2020), and the Baosteel-Australia Joint Research and Development Center (Baosteel Grant no. BA14006). The authors would like to thank Dr. T. Silver for critical reading of this manuscript.

Received: ((will be filled in by the editorial staff))

Revised: ((will be filled in by the editorial staff))

Published online: ((will be filled in by the editorial staff))

This article is protected by copyright. All rights reserved.

References

- [1] a) B. Dunn, H. Kamath, J.-M. Tarascon, *Science* **2011**, 334, 928; b) V. Etacheri, R. Marom, R. Elazari, G. Salitra, D. Aurbach, *Energy Environ. Sci.* **2011**, 4, 3243; c) D. Larcher, J. M. Tarascon, *Nat. Chem.* **2015**, 7, 19; d) M. V. Reddy, G. V. Subba Rao, B. V. R. Chowdari, *Chem. Rev.* **2013**, 113, 5364; e) C. Jiang, E. Hosono, H. Zhou, *Nano Today* **2006**, 1, 28.
- [2] a) R. Teki, M. K. Datta, R. Krishnan, T. C. Parker, T. M. Lu, P. N. Kumta, N. Koratkar, *Small* **2009**, 5, 2236; b) H. Wu, Y. Cui, *Nano Today* **2012**, 7, 414.
- [3] a) J. Yang, Y.-X. Wang, S.-L. Chou, R. Zhang, Y. Xu, J. Fan, W.-x. Zhang, H. Kun Liu, D. Zhao, S. Xue Dou, *Nano Energy* **2015**, 18, 133; b) X. Xiao, W. Zhou, Y. Kim, I. Ryu, M. Gu, C. Wang, G. Liu, Z. Liu, H. Gao, *Adv. Funct. Mater.* **2015**, 25, 1426; c) M. Zhou, X. Li, B. Wang, Y. Zhang, J. Ning, Z. Xiao, X. Zhang, Y. Chang, L. Zhi, *Nano Lett.* **2015**, 15, 6222.
- [4] a) J.-I. Lee, Y. Ko, M. Shin, H.-K. Song, N.-S. Choi, M. G. Kim, S. Park, *Energy Environ. Sci.* **2015**, 8, 2075; b) X. Huang, J. Yang, S. Mao, J. Chang, P. B. Hallac, C. R. Fell, B. Metz, J. Jiang, P. T. Hurley, J. Chen, *Adv. Mater.* **2014**, 26, 4326; c) A. Magasinski, P. Dixon, B. Hertzberg, A. Kvit, J. Ayala, G. Yushin, *Nat. Mater.* **2010**, 9, 353.
- [5] H. Kim, M. Seo, M. H. Park, J. Cho, *Angew. Chem., Int. Ed.* **2010**, 49, 2146.
- [6] H. Wu, G. Chan, J. W. Choi, I. Ryu, Y. Yao, M. T. McDowell, S. W. Lee, A. Jackson, Y. Yang, L. Hu, Y. Cui, *Nat. Nanotechnol.* **2012**, 7, 310.
- [7] B. Wang, X. Li, X. Zhang, B. Luo, Y. Zhang, L. Zhi, *Adv. Mater.* **2013**, 25, 3560.
- [8] a) X. Li, M. Gu, S. Hu, R. Kennard, P. Yan, X. Chen, C. Wang, M. J. Sailor, J. G. Zhang, J. Liu, *Nat. Commun.* **2014**, 5, 4105; b) M. Ge, Y. Lu, P. Ercius, J. Rong, X. Fang, M. Mecklenburg, C. Zhou, *Nano Lett.* **2014**, 14, 261.
- [9] a) N. Lin, Y. Han, L. Wang, J. Zhou, J. Zhou, Y. Zhu, Y. Qian, *Angew. Chem., Int. Ed.* **2015**, 54, 3822; b) J. Liu, P. Kopold, P. A. van Aken, J. Maier, Y. Yu, *Angew. Chem., Int. Ed.* **2015**, 54, 9632.
- [10] a) F. H. Du, B. Li, W. Fu, Y. J. Xiong, K. X. Wang, J. S. Chen, *Adv. Mater.* **2014**, 26, 6145; b) Z. Zhang, Y. Wang, W. Ren, Q. Tan, Y. Chen, H. Li, Z. Zhong, F. Su, *Angew. Chem., Int. Ed.* **2014**, 53, 5165.
- [11] a) J. Saint, M. Morcrette, D. Larcher, L. Laffont, S. Beattie, J. P. Pérès, D. Talaga, M. Couzi, J. M. Tarascon, *Adv. Funct. Mater.* **2007**, 17, 1765; b) S. H. Ng, J. Wang, D. Wexler, K. Konstantinov, Z. P. Guo, H. K. Liu, *Angew. Chem., Int. Ed.* **2006**, 45, 6896; c) Y.-X. Wang, J. Yang, S.-L. Chou, H. K. Liu, W.-x. Zhang, D. Zhao, S. X. Dou, *Nat. Commun.* **2015**, 6, 8689; d) N. Liu, Z. Lu, J. Zhao,

- M. T. McDowell, H. W. Lee, W. Zhao, Y. Cui, *Nat. Nanotechnol.* **2014**, *9*, 187; e) W. Luo, D. Shen, R. Zhang, B. Zhang, Y. Wang, S. X. Dou, H. K. Liu, J. Yang, *Adv. Funct. Mater.* **2016**, *26*, 7800; f) W. Luo, Y. Wang, L. Wang, W. Jiang, S.-L. Chou, S. X. Dou, H. K. Liu, J. Yang, *ACS Nano* **2016**, *10*, 10524.
- [12] a) I. H. Son, J. Hwan Park, S. Kwon, S. Park, M. H. Rummeli, A. Bachmatiuk, H. J. Song, J. Ku, J. W. Choi, J. M. Choi, S. G. Doo, H. Chang, *Nat. Commun.* **2015**, *6*, 7393; b) R. Zhang, Y. Du, D. Li, D. Shen, J. Yang, Z. Guo, H. K. Liu, A. A. Elzatahry, D. Zhao, *Adv. Mater.* **2014**, *26*, 6749; c) W. Luo, Y. Wang, S. Chou, Y. Xu, W. Li, B. Kong, S. X. Dou, H. K. Liu, J. Yang, *Nano Energy* **2016**, *27*, 255.
- [13] J. Zhao, Z. Lu, N. Liu, H. W. Lee, M. T. McDowell, Y. Cui, *Nat. Commun.* **2014**, *5*, 5088.
- [14] a) Z. Wang, X. W. D. Lou, *Adv. Mater.* **2012**, *24*, 4124; b) H. Wang, D. Ma, X. Huang, Y. Huang, X. Zhang, *Sci. Rep.* **2012**, *2*, 701; c) M. Dahl, Y. Liu, Y. Yin, *Chem. Rev.* **2014**, *114*, 9853.
- [15] E. M. Lotfabad, P. Kalisvaart, K. Cui, A. Kohandehghan, M. Kupsta, B. Olsen, D. Mitlin, *Phys. Chem. Chem. Phys.* **2013**, *15*, 13646.
- [16] a) M. Li, X. Li, W. Li, X. Meng, Y. Yu, X. Sun, *Electrochem. Commun.* **2015**, *57*, 43; b) T. Zhou, Y. Zheng, H. Gao, S. Min, S. Li, H. K. Liu, Z. Guo, *Adv. Sci.* **2015**, *2*, 1500027.
- [17] W. Li, J. Yang, Z. Wu, J. Wang, B. Li, S. Feng, Y. Deng, F. Zhang, D. Zhao, *J. Am. Chem. Soc.* **2012**, *134*, 11864.
- [18] M. Wagemaker, R. van de Krol, A. P. Kentgens, A. A. Van Well, F. M. Mulder, *J. Am. Chem. Soc.* **2001**, *123*, 11454.
- [19] a) L. Yu, H. Hu, H. B. Wu, X. W. D. Lou, *Adv. Mater.* **2017**, DOI: 10.1002/adma.201604563; b) T. Bok, S. Choi, J. Lee, S. Park, *J. Mater. Chem. A* **2014**, *2*, 14195; c) S. Zeng, D. Liu, Y. Chen, J. Qian, Y. Cao, H. Yang, X. Ai, *J. Mater. Chem. A* **2015**, *3*, 9938; d) W. Xiao, J. Zhou, L. Yu, D. Wang, X. W. D. Lou, *Angew. Chem., Int. Ed.* **2016**, *55*, 7427; e) B. Y. Guan, L. Yu, J. Li, X. W. D. Lou, *Sci. Adv.* **2016**, *2*, e1501554; f) E. M. Lotfabad, P. Kalisvaart, A. Kohandehghan, K. Cui, M. Kupsta, B. Farbod, D. Mitlin, *J. Mater. Chem. A* **2014**, *2*, 2504.

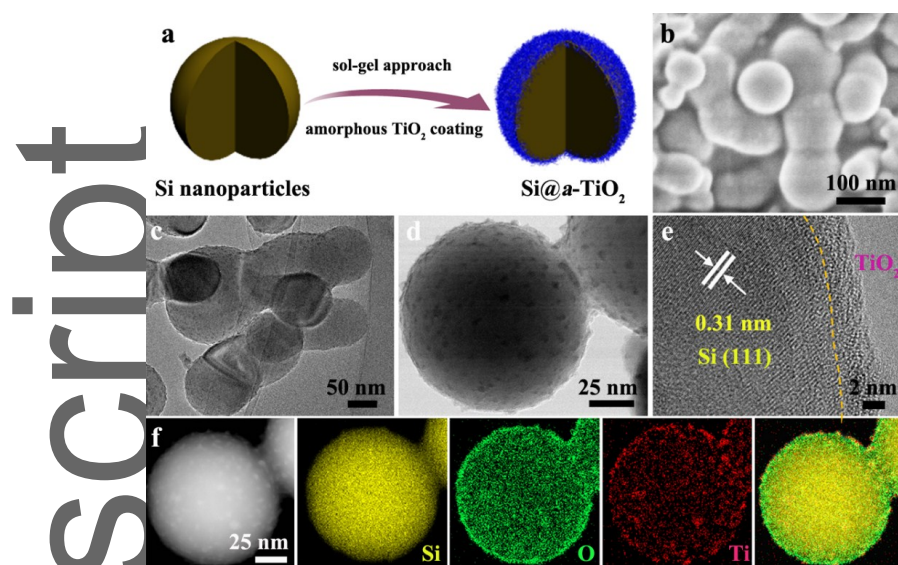


Figure 1. (a) Schematic illustration of fabrication process for the amorphous TiO₂ coated Si core-shell nanoparticles. (b) FESEM, (c, d) TEM, and (e) HR-TEM images of Si@a-TiO₂ nanoparticles. (f) Scanning TEM image and the corresponding EDS mapping images of elemental Si, O, and Ti for a single Si@a-TiO₂ nanoparticle.

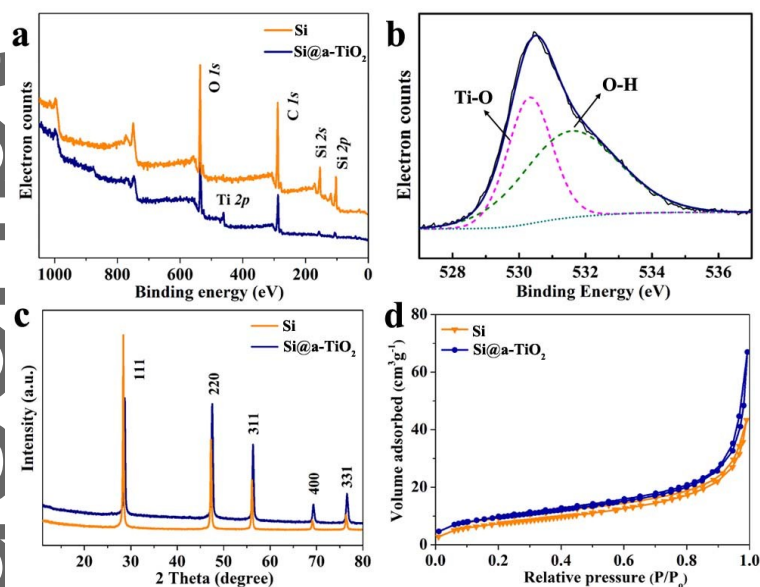


Figure 2. Physicochemical properties of the amorphous TiO_2 coated commercial Si nanoparticles. (a) XPS survey spectra of the pristine commercial Si and Si@a- TiO_2 nanoparticles. (b) O 1s high-resolution XPS spectrum of Si@a- TiO_2 nanoparticles. (c) XRD patterns and (d) nitrogen sorption isotherms of the pristine Si and Si@a- TiO_2 nanoparticles.

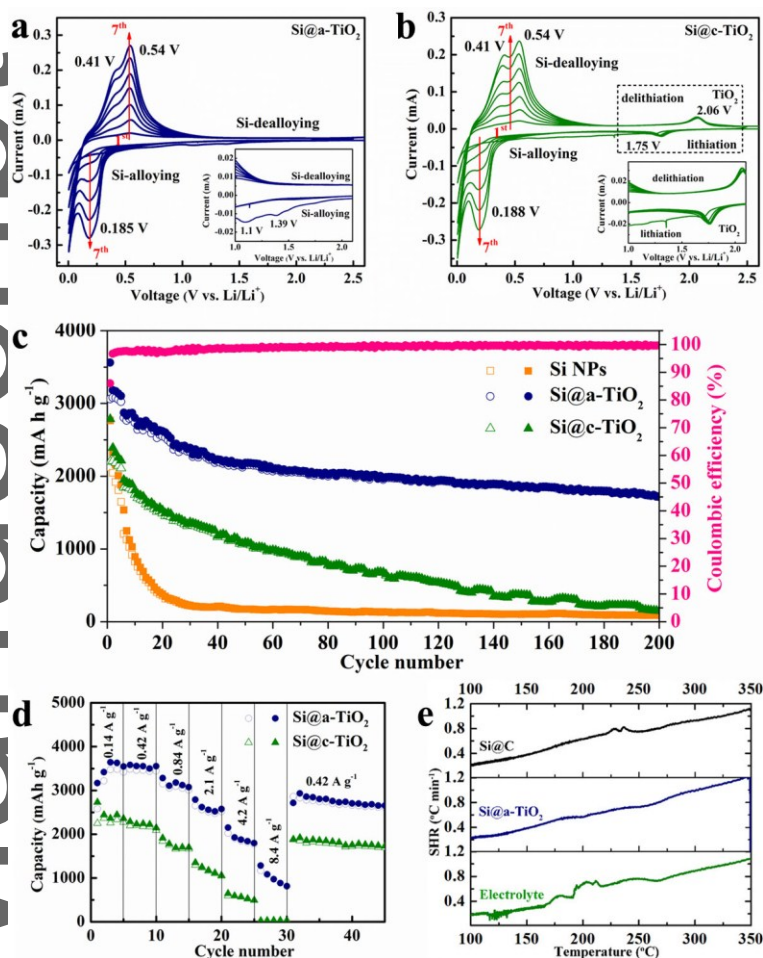


Figure 3. Electrochemical performances of the amorphous TiO₂ coated commercial Si nanoparticles as anode in lithium ion batteries. CV curves of (a) the Si@a-TiO₂ and (b) Si@c-TiO₂ nanoparticles at a scanning rate of 0.01 mV s⁻¹ in the voltage range from 0.005 to 2.5 V (insets: enlargements of indicated voltage ranges). (c) Cycling performance of the pristine Si, Si@a-TiO₂ and Si@c-TiO₂ nanoparticle electrodes at a current density of 420 mA·g⁻¹ (first activated with five cycles at 140 mA·g⁻¹). (d) Comparison of the rate capabilities of Si@a-TiO₂ and Si@c-TiO₂ nanoparticle electrodes at different current densities. (e) The safety properties of Si@a-TiO₂ and Si@C core-shell nanoparticle anodes as determined by the self-heating rate (SHR). The battery safety was estimated by accelerating rate calorimetry, in which the electrode samples were discharged to 0.001 V and tested over a temperature range from 90 to 350 °C. All the capacities of cells have been normalized based on the weight of active materials in the pristine Si, Si@a-TiO₂ and Si@c-TiO₂ nanoparticles, respectively.

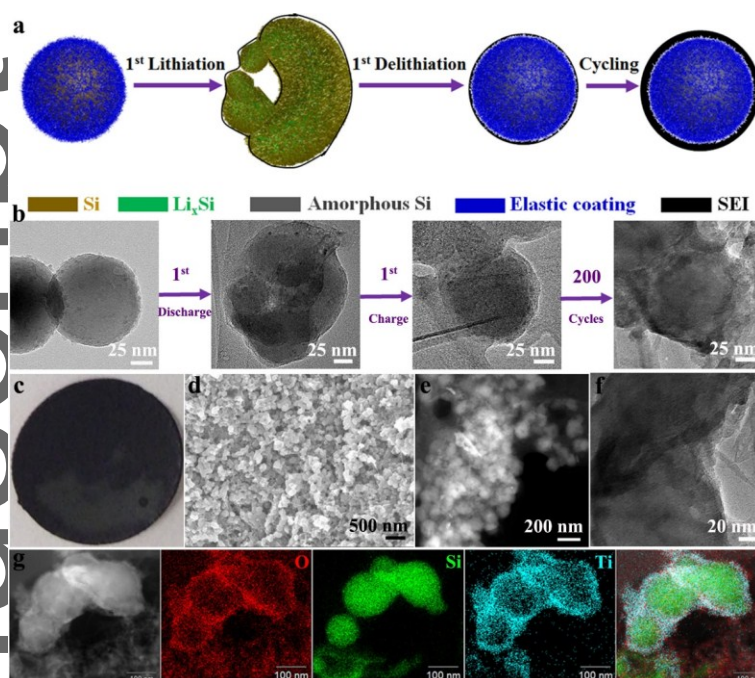


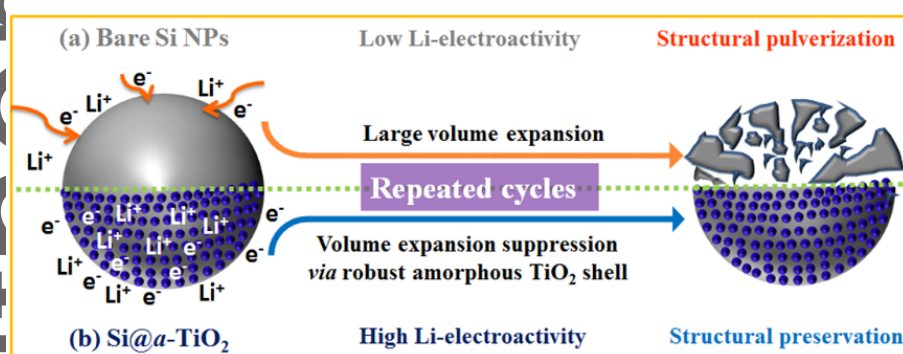
Figure 4. Structural evolution of the amorphous TiO₂ coated commercial Si nanoparticle electrode during electrochemical cycling. (a) Schematic illustration showing the structural maintenance of the Si@a-TiO₂ nanoparticle electrode during lithium insertion and extraction, combined with the corresponding TEM images (b). (c) Optical, (d) FESEM, (e) dark field TEM, (f) TEM, and (g) STEM images and elemental mapping of O, Si, and Ti for the Si@a-TiO₂ nanoparticle electrode after 200 cycles.

Amorphous TiO₂-encapsulated commercial Si nanoparticle core-shell structures deliver superior electrochemical performance and high-safety lithium storage. The amorphous TiO₂ shells can offer superior buffering properties and achieve excellent lithium storage properties with high initial Coulombic efficiency, long-term cycling stability, and greater safety.

Key Word: Core-shell structure, sol-gel coating, titanium oxide, lithium ion batteries, silicon nanoparticles

Jianping Yang, Yunxiao Wang, Wei Li, Lianjun Wang, Yuchi Fan, Wan Jiang, Wei Luo,* Yang Wang, Biao Kong, Cordelia Selomulya, Hua Kun Liu, Shi Xue Dou and Dongyuan Zhao*

Amorphous TiO₂ Shells: A Vital Elastic Buffering Layer on Silicon Nanoparticles for High-Performance and Safe Lithium Storage



((Supporting Information can be included here using this template))

Copyright WILEY-VCH Verlag GmbH & Co. KGaA, 69469 Weinheim, Germany, 2016.

Supporting Information

Amorphous TiO₂ Shells: A Vital Elastic Buffering Layer on Silicon Nanoparticles for High-Performance and Safe Lithium Storage

Jianping Yang, Yunxiao Wang, Wei Li, Lianjun Wang, Yuchi Fan, Wan Jiang, Wei Luo, Yang Wang, Biao Kong, Cordelia Selomulya, Hua Kun Liu, Shi Xue Dou and Dongyuan Zhao**

Dr. J. P. Yang, Prof. L. J. Wang, Dr. Y. C. Fan, Prof. W. Jiang, Dr. W. Luo,

State Key Laboratory for Modification of Chemical Fibers and Polymer Materials, College of Materials Science and Engineering, Donghua University, Shanghai 201620, P. R. China.

E-mail: wluo@dhu.edu.cn

Dr. Y. X. Wang, Prof. H. K. Liu, Prof. S. X. Dou

Institute for Superconducting & Electronic Materials, Australian Institute of Innovative Materials, University of Wollongong, Innovation Campus, Squires Way, North Wollongong, NSW 2500, Australia

This article is protected by copyright. All rights reserved.

Dr. W. Li, Prof. D. Y. Zhao

Department of Chemistry, Laboratory of Advanced Materials, Fudan University, Shanghai 200433, P.
R. China

E-mail: dyzhao@fudan.edu.cn

Y. Wang, Dr. B. Kong, Prof. C. Selomulya, Prof. D. Y. Zhao

Department of Chemical Engineering, Monash University, Clayton, Victoria 3800, Australia

Author Manuscript

1. Experimental Section

Synthesis of Si@a-TiO₂ Core-Shell Nanoparticles: The amorphous TiO₂ layers were deposited on the surface of the commercial silicon nanoparticles *via* a modified kinetics-controlled sol-gel coating approach. In a typical procedure, 0.45 g of commercial silicon nanoparticles with diameters of ~ 100 nm (purchased from Nanostructured and Amorphous Materials, Inc.) were added into a mixed solution containing 600 mL of absolute ethanol and 1.8 mL of ammonia aqueous solution (28 wt %). The mixture became a uniformly dispersed solution after treatment with ultrasound for 30 min and stirring at 40 °C for 30 min. Afterwards, 4 mL of titanium isopropylate was added dropwise and the mixture was reacted at 40 °C for 40 h under gentle stirring (200 rpm). The amorphous TiO₂ coated silicon core-shell nanoparticles were obtained after centrifugation and washing with ethanol for several times, before drying at 80 °C for 12 h. Accordingly, the crystalline TiO₂ coated silicon core-shell nanoparticles (Si@c-TiO₂) were obtained after sintering in nitrogen at 450 °C for 5 h as the contrast sample.

Synthesis of Si@C Core-Shell Nanoparticle: The carbon layer with a shell thickness of ~ 3nm was fabricated *via* a sol-gel polymerization process by using resorcinol-formaldehyde resin polymer as a carbon source according to a previous report.^[1] The Si@C core-shell nanoparticles are obtained after calcination in nitrogen atmosphere at 700 °C for 3 h.

Characterization: The nanostructures and elemental mappings were further investigated by transmission electron microscopy (TEM, JEOL JEM-ARM200F). The samples were suspended in ethanol and dried on a holey carbon support film on a Cu grid for TEM measurements. The

morphologies of the samples were observed on a Hitachi S-4800 (Japan) field-emission scanning electron microscope (FESEM). The crystal structure and phase of products were characterized using wide-angle X-ray diffraction (XRD, Bruker D8, Germany) with Ni-filtered Cu K α radiation (40 kV, 40 mA). The porosity was measured by nitrogen sorption isotherms at 77 K with a Micromeritics Tristar 3020 analyzer (USA). Before measurements, the samples were degassed in vacuum at 180 °C for at least 6 h. The Brunauer-Emmett-Teller (BET) method was utilized to calculate the specific surface areas (S_{BET}), using adsorption data in a relative pressure (P/P_0) range from 0.04 to 0.2. The pore volume and pore size distributions were derived from the adsorption branches of isotherms by using the Barrett-Joyner-Halenda (BJH) model. The total pore volume, V_t , was estimated from the amount adsorbed at a relative pressure P/P_0 of 0.995. X-ray photoelectron spectroscopy (XPS) was conducted on a RBD upgraded PHI-5000C ESCA system (Perkin Elmer) with Mg K α radiation ($h\nu = 1253.6$ eV). All binding energies were calibrated by using the carbon contaminant (C 1s = 284.6 eV).

Electrochemical testing: The electrochemical measurements were conducted by assembling coin-type half cells in an argon-filled glove box. The electrode slurry was prepared by mixing 60 wt. % active material (Si nanoparticles (NPs), Si@a-TiO₂, Si@c-TiO₂), 10 wt. % Super P[®], 10 wt. % multi-walled carbon nanotubes, and 20 wt. % carboxymethyl cellulose (CMC) in a planetary mixer (KK-250S). The electrode films were prepared by pasting the slurry on copper foil using a doctor blade to a thickness of 100 μm , which was followed by drying in a vacuum oven at 80 °C overnight. The working electrodes were prepared by punching the electrode film into discs 0.95 cm in diameter. Lithium foil was employed for both reference and counter electrodes. The electrodes were separated by a Celgard separator. The electrolyte was 1.0 M LiPF₆ in 3:4:3 (weight ratio) ethylene carbonate (EC)/dimethyl carbonate (DMC)/diethylene carbonate (DEC), with 5 wt. % fluoroethylene

carbonate (FEC) additive from Novolyte Technologies. The electrochemical performances were tested with a Land Battery Test System with a cut-off voltage range from 0.005 to 2.5 V (vs. Li /Li⁺). All the capacities of cells were normalized based on the weight of active materials in the pristine Si, Si@a-TiO₂, and Si@c-TiO₂ nanoparticles, respectively. Cyclic voltammetry and impedance tests were performed using a Biologic VMP-3 electrochemical workstation from 0.005 to 2.5 V at a sweep rate of 0.01 mV·s⁻¹. The mass loading of Si@a-TiO₂ electrode was ~ 0.44 mg on each electrode disc (0.708 cm²), corresponding an areal loading of 0.621 mg/cm². The battery safety of Si@a-TiO₂ and Si@C was tested by accelerating rate calorimetry (ARC). Pellet-electrode coin cells were discharged to 0.001 V, and the electrode materials were collected by disassembling the discharged coin cells in an Ar-filled glove box. The obtained electrode was then washed 3 times using DEC and dried in the vacuum antechamber of the glove box overnight. 150 mg of lithiated electrode powder and 150 mg of electrolyte were put into a bomb tube for the ARC testing. The ARC test temperature range was set from 90 to 350 °C.

Reference:

- [1] W. Luo, Y. Wang, S. Chou, Y. Xu, W. Li, B. Kong, S. X. Dou, H. K. Liu, J. Yang, *Nano Energy* **2016**, *27*, 255.

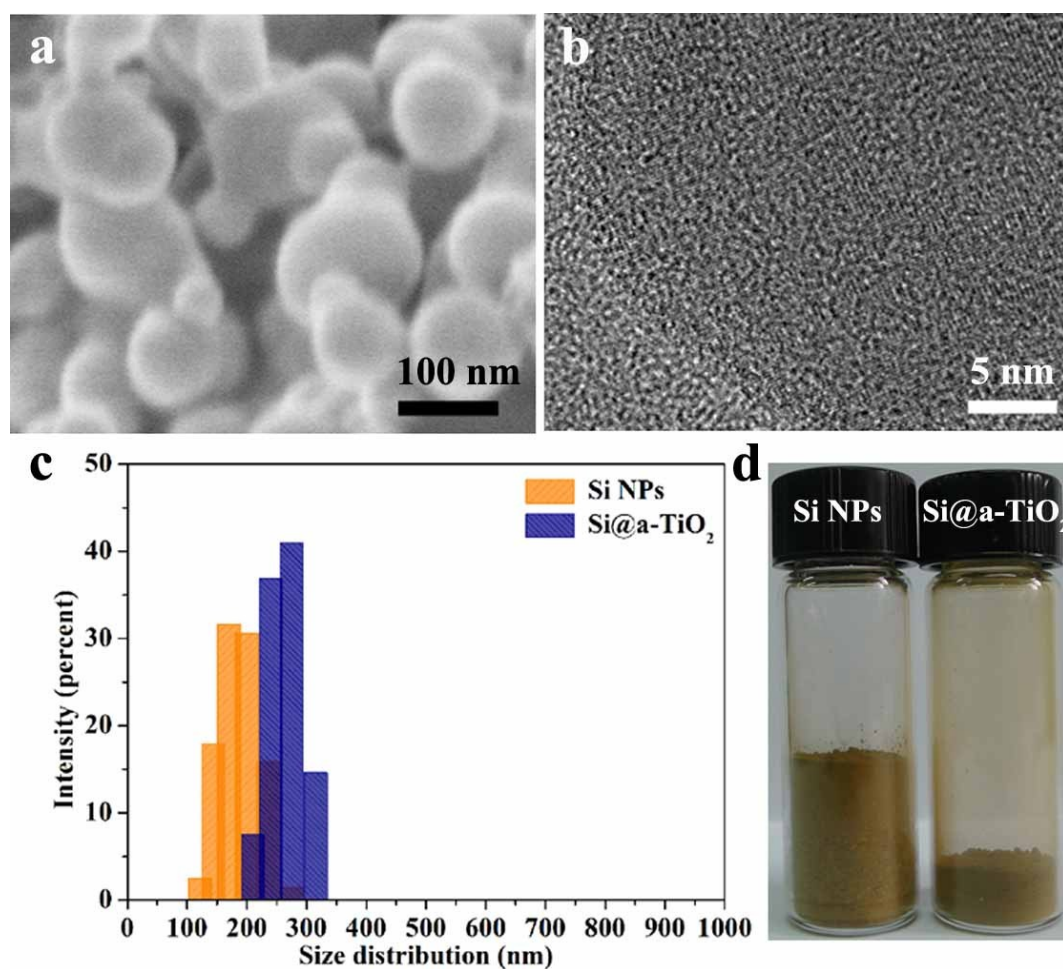


Figure S1. (a) FESEM and (b) HRTEM images of the pristine Si nanoparticles. (c) Dynamic light scattering (DLS) measurements of the pristine Si and Si@a-TiO₂ nanoparticles. (d) Photographs of the pristine Si and Si@a-TiO₂ nanoparticles in vials containing 0.3 g of tightly packed powder.

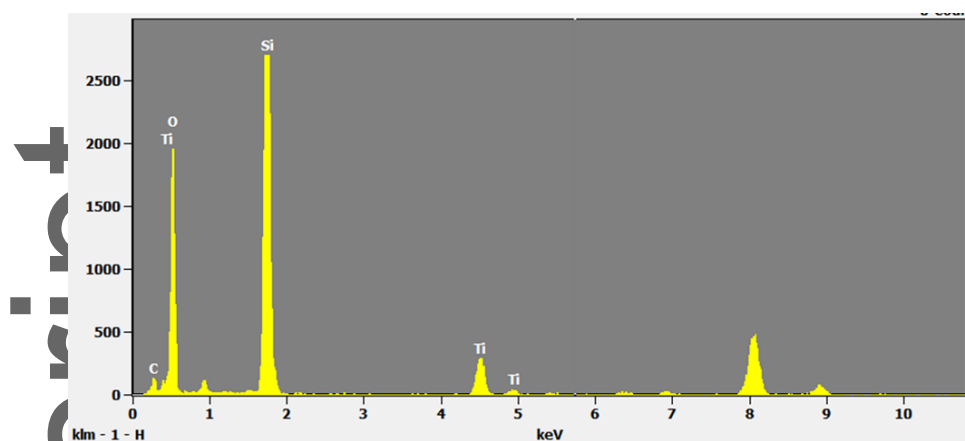


Figure S2. Energy-dispersive X-ray spectrum of the core-shell Si@a-TiO₂ nanoparticles.

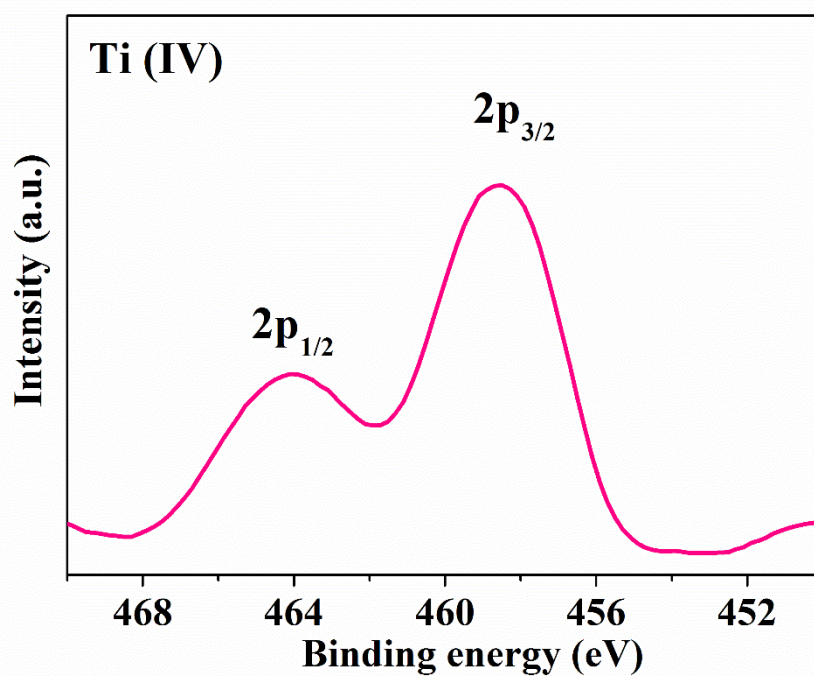


Figure S3. XPS spectrum of Ti 2p peaks for the core-shell Si@a-TiO₂ nanoparticles. The peaks centered at 458.5 and 464.2 eV are well assigned to Ti 2p_{3/2} and 2p_{1/2} of TiO₂, respectively, revealing that Ti in the TiO₂ shells is in the form of Ti⁴⁺.

Author Manuscript

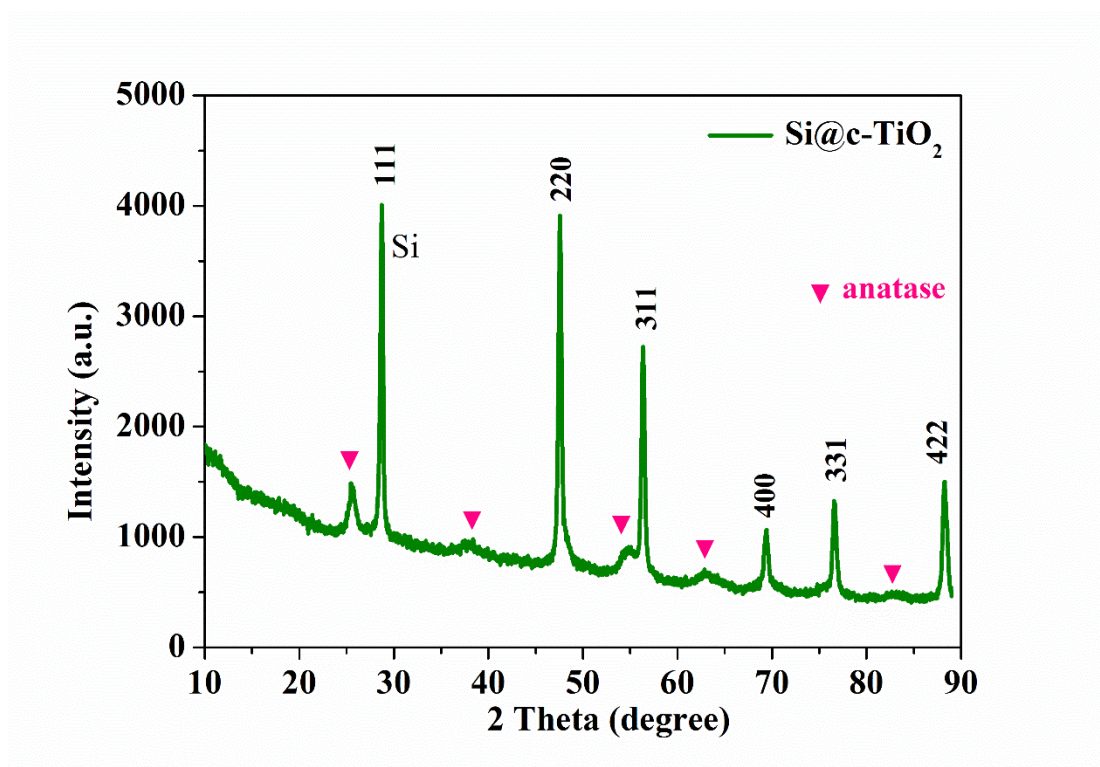


Figure S4. XRD pattern of the crystalline TiO₂ coated silicon core-shell (Si@c-TiO₂) nanoparticles, which were obtained after sintering the of Si@ α -TiO₂ samples in nitrogen at 450 °C for 5 h.

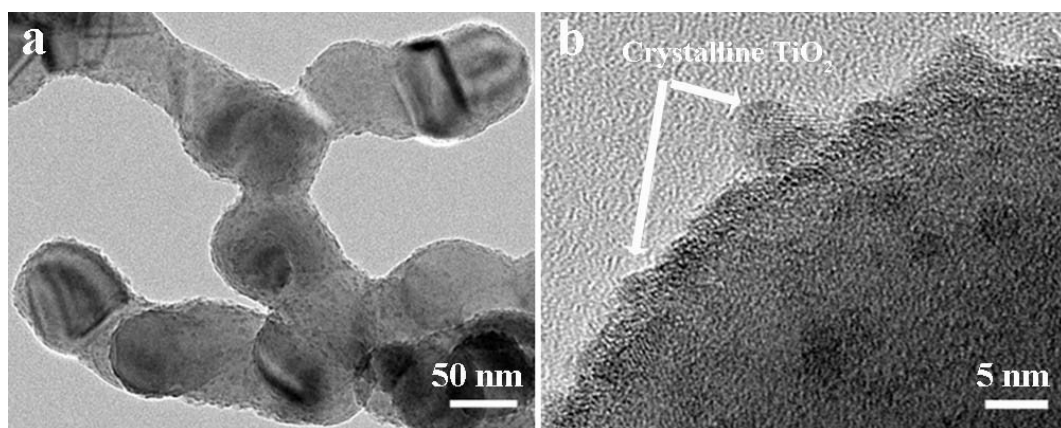


Figure S5. TEM images of the crystalline TiO₂ coated silicon core-shell (Si@c-TiO₂) nanoparticles, which were obtained after sintering of Si@a-TiO₂ samples in nitrogen at 450 °C for 5 h.

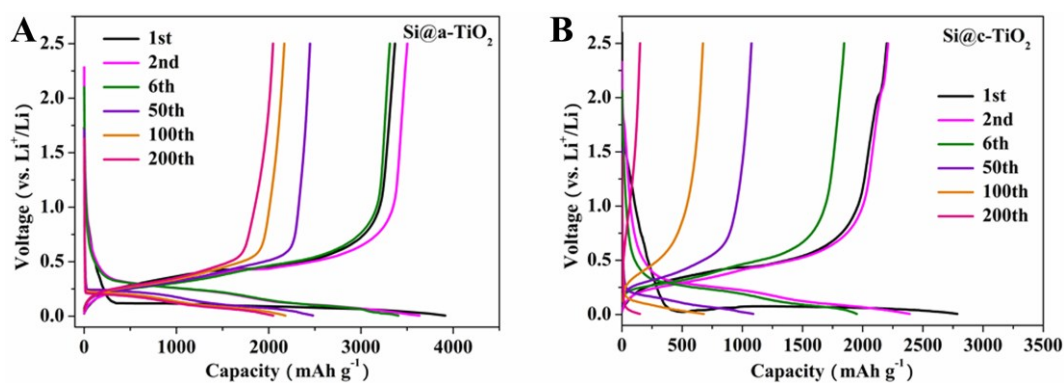


Figure S6. Galvanostatic charge-discharge profiles of the Si@a-TiO₂ (A) and Si@c-TiO₂ (B) nanoparticle electrodes at various cycles at a current density of 420 mA·g⁻¹ (first activated with five cycles at 140 mA·g⁻¹).

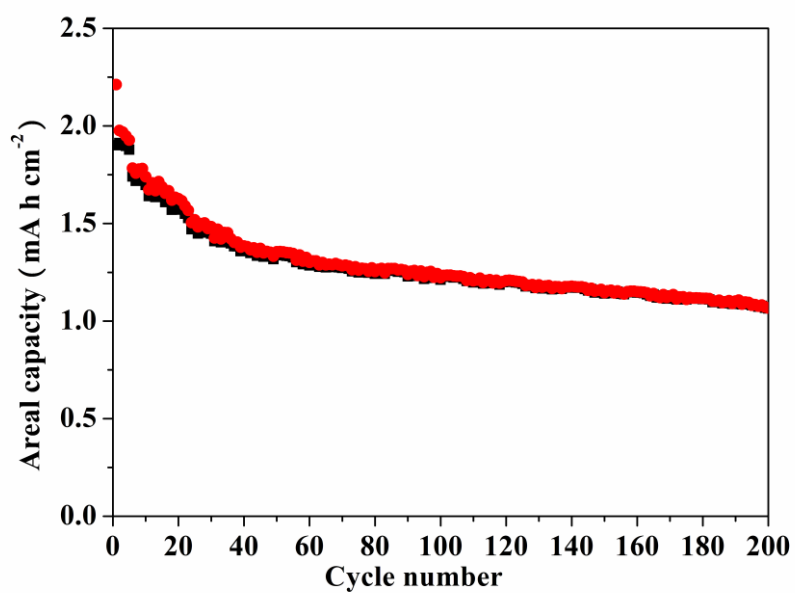


Figure S7. Areal capacity of Si@a-TiO₂ electrode over 200 cycles.

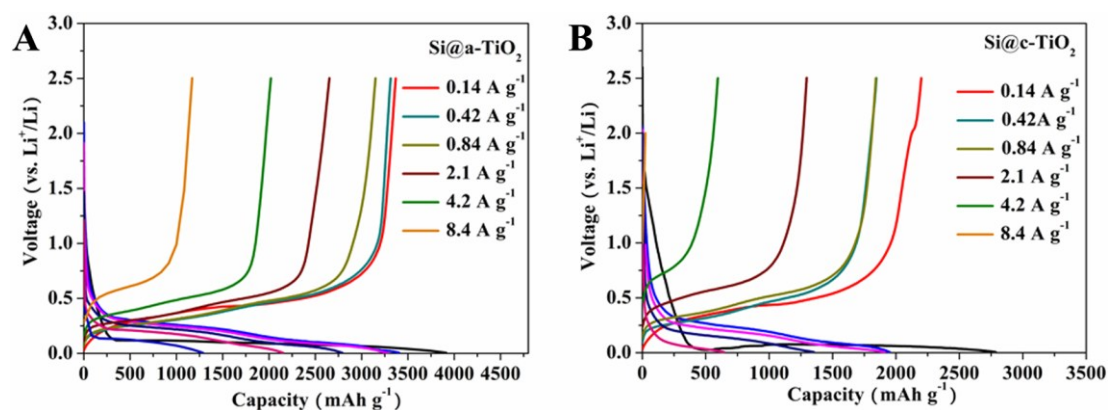


Figure S8. Galvanostatic charge-discharge profiles of the Si@a-TiO₂ (A) and Si@c-TiO₂ (B) nanoparticle electrodes at various current density.

Table S1. Comparison of the synthesis method, silicon content, mass areal loading, initial

Coulombic efficiency (ICE) and electrochemical performance of graphene, silica, and polymer coated silicon composites.

Sample	Synthesis method	Si (wt %)	Mass areal loading (mgcm ⁻²)	ICE (%)	Current density (mA g ⁻¹)	Capacity after 200 cycles (mA h g ⁻¹)
Si@a-TiO ₂ nanoparticles (This work)	sol-gel at 40 °C No annealing	89	0.621	86.1	420	~ 1720
Graphene-coated Si microparticles	multi-steps of surface	91	0.8	93.2	2100	~ 1600

(Nat. Energy 2016, 15029)	modification, coating, etching annealing at 450 °C					
Bulk@nanowire Si@SiO _x @C (Adv. Mater. 2013, 25, 4498)	750 °C-850 °C, O ₂ stream treatment before carbon coating	/	2	92	420	< 1700
Si NPs@ conducting polymer (Nat. Commun. 2013, 4:1943)	in-situ polymerization of aniline monomer to form PANi hydrogel	75	0.2	70	1000	< 1700

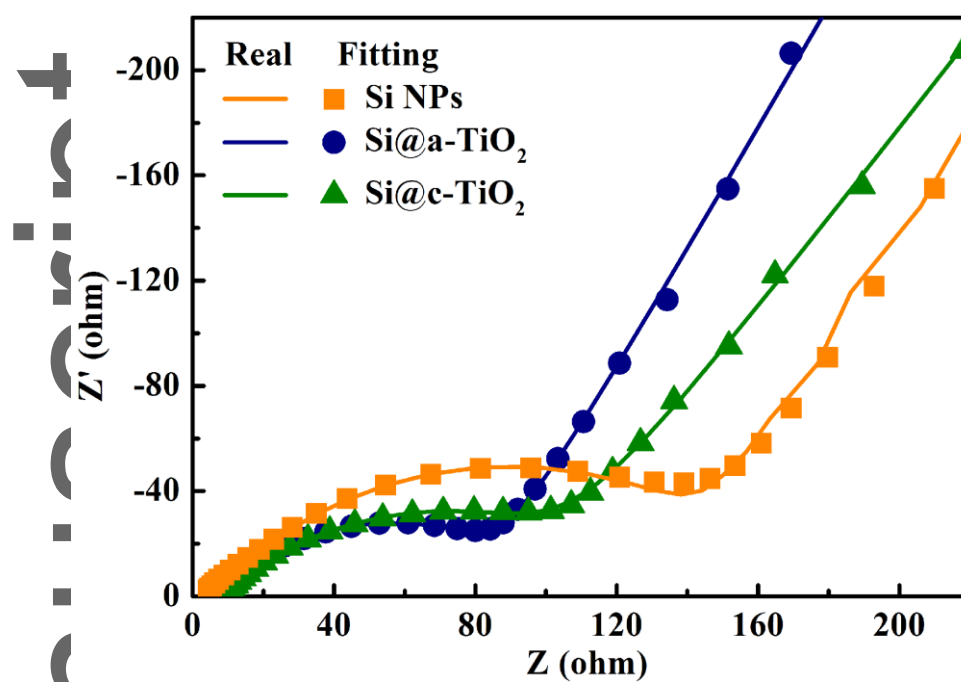


Figure S9. Impedance spectra measured after rate capability test of the Si, Si@a-TiO₂ and Si@c-TiO₂ nanoparticle electrodes.

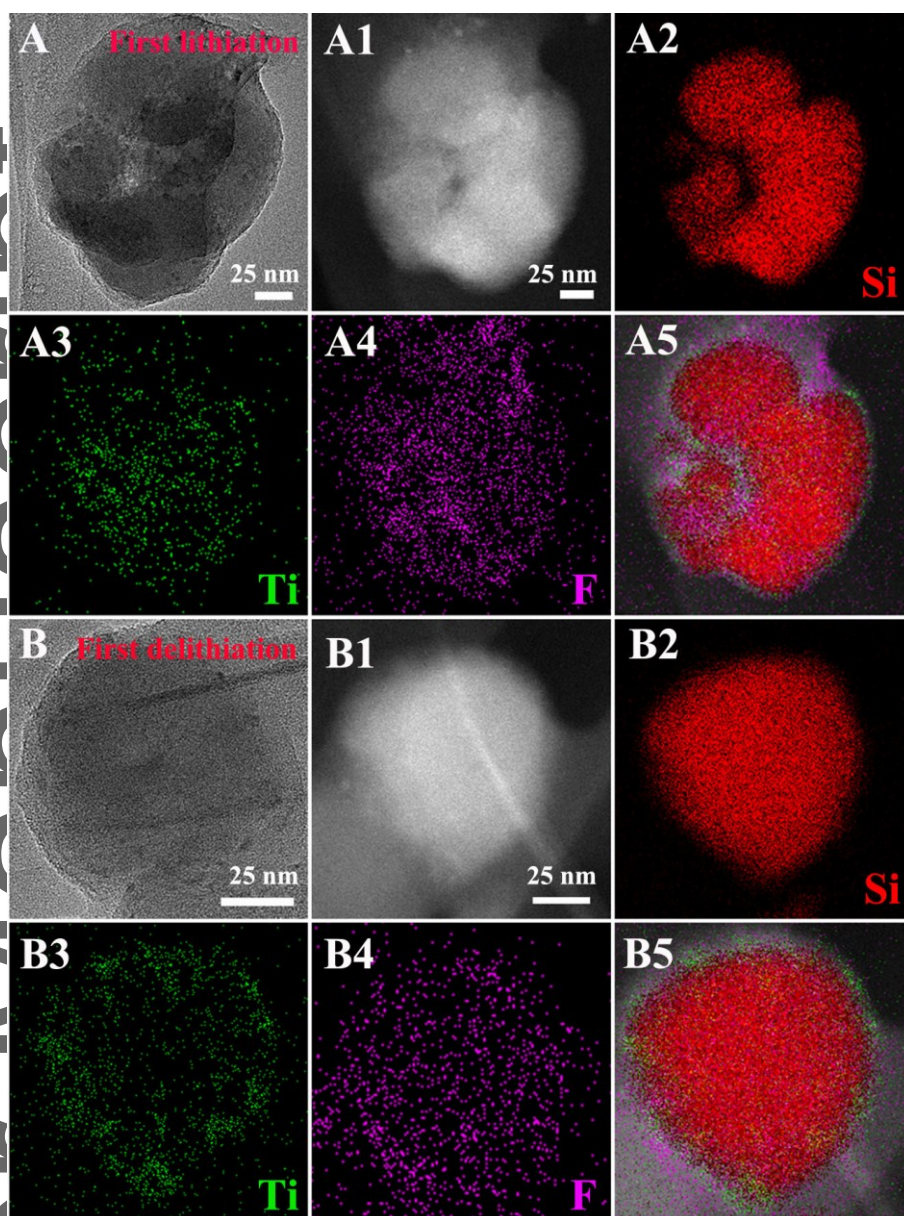


Figure S10. (A, B) Ex-situ TEM images, (A1, B1) STEM images, and (A2-A5, B2-B5) elemental mapping of Si, Ti, and F for a single Si@ α -TiO₂ nanoparticle during the first lithium insertion (A-A5) and delithiation (B-B5) processes.

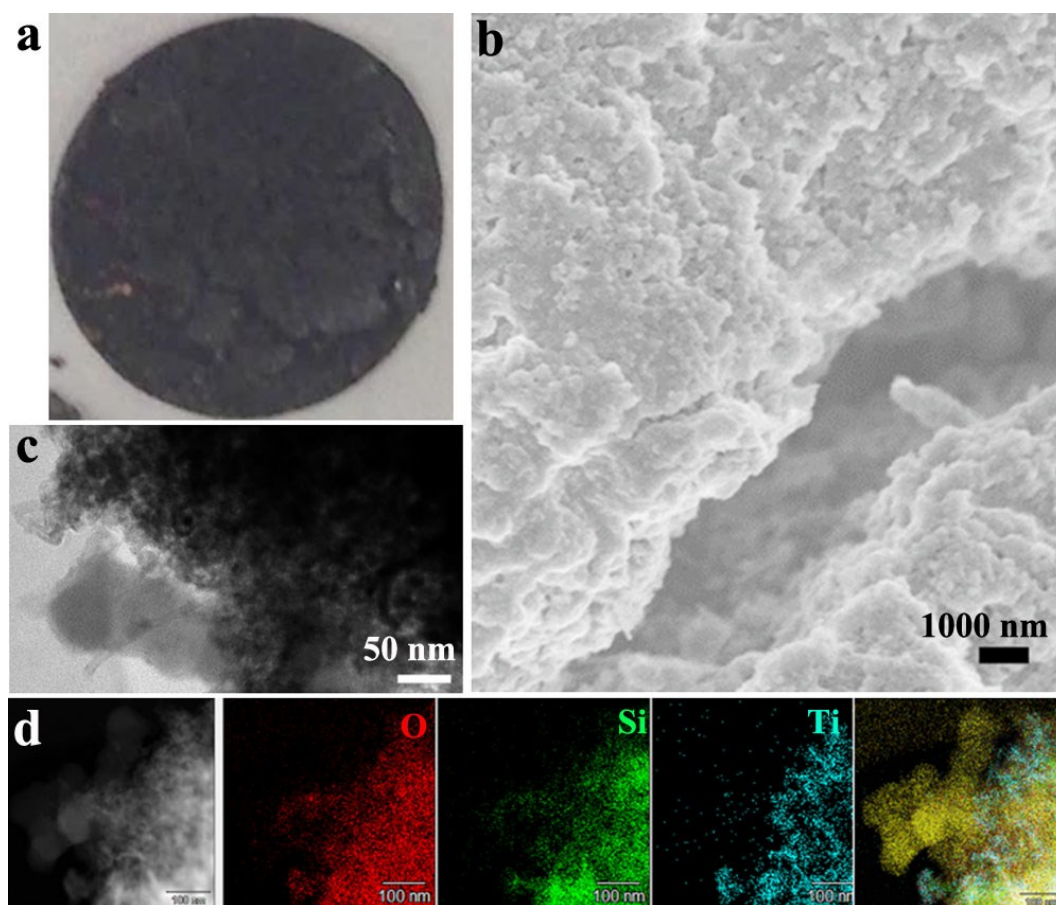


Figure S11. (a) Optical photograph, (b) FESEM and (c) TEM images, and (d) STEM images and elemental mapping of O, Si, and Ti for the crystalline TiO₂ coated silicon core-shell (Si@c-TiO₂) nanoparticle electrode after 200 cycles, indicating structural pulverization.

Author

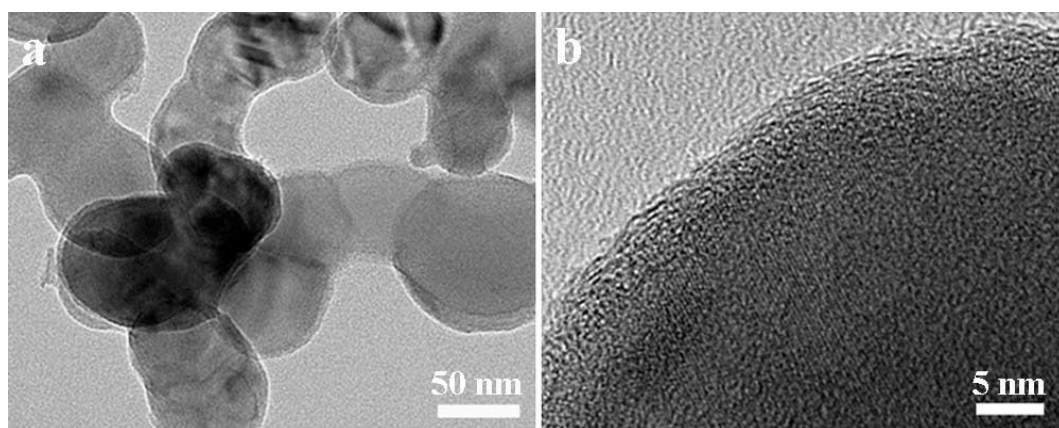


Figure S12. TEM images of the silicon nanoparticles encapsulated by carbon with shell thickness of ~ 3 nm (Si@C). The carbon shells were coated on the Si surface *via* a sol-gel polymerization process using resorcinol-formaldehyde (RF) resin polymer as a carbon source and calcined in nitrogen at 700 °C for 3 h.